Dynamic Viscous Simulations of Atmospheric-Entry Capsules

Scott M. Murman[*]

NASA Ames Research Center, Moffett Field, CA, USA

Abstract

Viscous, free-oscillation simulations with the Overflow solver are used to predict the aerodynamic behavior of non-lifting capsule shapes in the supersonic speed regime. Computations using hybrid Reynolds-averaged Navier-Stokes turbulence models are examined for two novel atmospheric-entry capsule configurations: an idealized inflatable decelerator concept, and the Orion Crew Module. The simulation results are validated against nonlinear aerodynamic models determined from free-flight ballistic-range data analysis. For the Orion Crew Module, two separate methods of reducing identical range data, along with common models tested in separate range facilities, are included. The computations demonstrate the efficiency and accuracy of dynamic simulations for developing a nonlinear aerodynamic performance database. Analysis indicates that the typical nonlinear, bluff-body behavior is characterized by a rate-dependent dynamic response, which is not currently accounted for in common aerodynamic models.

Nomenclature

α	angle of attack (deg)
β	angle of sideslip (deg)
δ_i	control surface settings
$\dot{\alpha}, \dot{\beta}$	rate of change of α and β
μ	molecular viscosity
ν	kinematic viscosity
σ	standard deviation
a	sonic speed

[*]Aerospace Engineer, Member AIAA. Scott.M.Murman@nasa.gov

American Institute of Aeronautics and Astronautics

M	Mach number
p, q, r	roll, pitch, and yaw rates
Re	Reynolds number
t	time
C_A, C_N, C_Y	axial, normal, and lateral force coefficients
C_l, C_m, C_n	roll, pitch, and yaw moment coefficients
$\mathcal{V}$	cell volume

Vector Quantities

$\boldsymbol{\eta}$	dynamic aerodynamic parameters
$\boldsymbol{\kappa}$	finite-difference grid metrics
$\boldsymbol{\xi}$	static aerodynamic parameters
$\boldsymbol{e}$	error
$\boldsymbol{u}$	velocity
$\boldsymbol{C}_F$	aerodynamic loads

Subscripts

∞	freestream
d	dynamic derivative
o	base state
s	static derivative
t	turbulent quantity
tot	total (axisymmetric) angle

1 Introduction

Computational Fluid Dynamics (CFD) is a key technology in the design of NASA's Orion Crew Module (CM) entry capsule, and the development of novel high-mass decelerator concepts for future Mars missions. Atmospheric-entry capsule and probe shapes provide a challenge for numerical analysis due to the inevitable separation and bluff-body shedding over the aft end of the vehicle. This same unsteady physics creates difficulties for stability and control, as the pitch damping is adversely effected when it is most needed to damp the oscillations due to the unsteady wake. Further, accurately determining the pitch damping from experimental measurements for capsule and probe shapes has been a challenge dating back to the Apollo and Viking programs (cf. [1–7]). This paper uses viscous, moving-body (free-oscillation) CFD simulations to predict the aerodynamic behavior of capsule shapes in the supersonic speed regime.

American Institute of Aeronautics and Astronautics

These simulations provide both the static and dynamic coefficients needed for accurate aerodynamic modeling of performance, risk assessment, targeting, etc.

Previous work utilized an automated, Cartesian-mesh-based, inviscid flow solver to perform a dynamic analysis for the Viking, Mars Exploration Rover (MER), and Genesis Sample-return Capsule (SRC) at supersonic flow conditions[8]. This work extends that effort to viscous, Reynolds-averaged Navier-Stokes (RANS) simulations of two novel capsule shapes using the Overflow solver[9–11], and validates the results against recent free-flight ballistic-range data. The configurations analyzed are an inflatable aerodynamic decelerator (IAD) concept for Mars entry developed by NASA's Program to Advance Inflatable Decelerators for Atmospheric Entry (PAI-DAE)[12], and the Orion CM[13–15]. The former is referred to herein as simply the "PAI-DAE configuration", and is modeled as a rigid aeroshell to match the rigid ballistic range test model. The outer mold line for these configurations is presented in Fig. 1. Both are analyzed at supersonic, ballistic-entry (non-lifting) conditions.
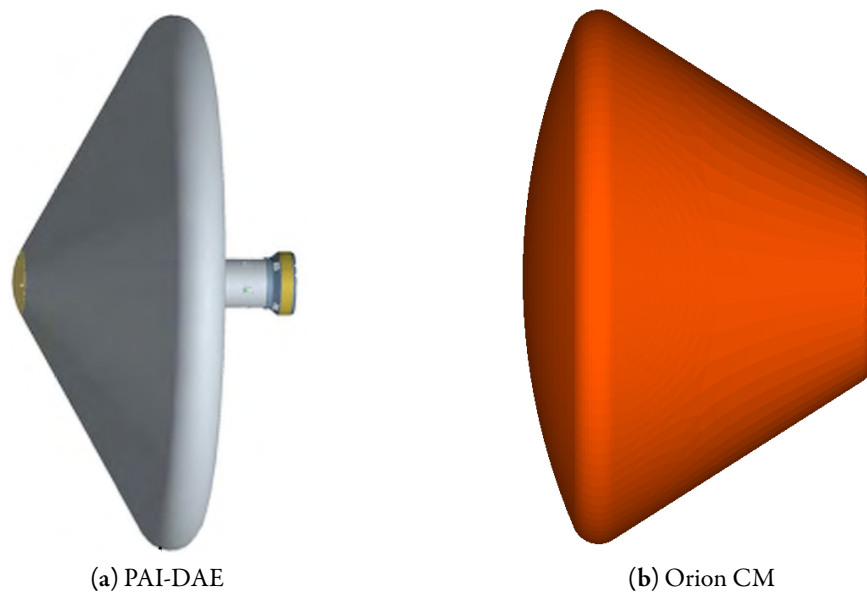

(a) PAI-DAE   (b) Orion CM

Figure 1: Outer mold lines for the atmospheric-entry capsule shapes analyzed in this work. These shapes correspond to idealized, sub-scale ballistic-range models[12, 13].

In order to generate aerodynamic coefficient data from free-flight testing, an *a priori* assumption of the aerodynamic model (i.e. parameter and system identification) is necessary. This modeling effort is combined with regression methods to reduce free-flight observations (position and orientation) to aerodynamic coefficients. These modeling and regression choices are not unique however, and the issues associated with aerodynamic modeling of ballistic range experiments *viz.* the validation of simulation results must be considered. The paper thus begins with a review of aerodynamic modeling, focusing on the anal-

American Institute of Aeronautics and Astronautics

ysis of supersonic bluff-bodies, and the methods used in both ballistic range and CFD data reduction.

The discussion continues with a brief overview of the numerical approach, followed by analyses of the PAI-DAE and Orion capsules using hybrid-RANS simulation methods, and comparison with free-flight range data. A summary of the current work and some topics for future research concludes the paper. A self-contained appendix summarizes a novel method of specifying the numerical timestep in viscous simulations for the Overflow solver, which is of general utility, but especially relevant for dynamic simulations.

2   Aerodynamic Modeling

The aerodynamic characteristics of an aircraft are typically described by the force and moment coefficients about the body axes: the axial, normal, and lateral force coefficients (C_A, C_N, C_Y), and the roll, pitch, and yaw moment coefficients (C_l, C_m, C_n). Adopting a vector notation, the body force and moments are

$$\hat{\boldsymbol{C}}_F = [C_A, C_N, C_Y, C_l, C_m, C_n]^T \tag{1}$$

In this work the aerodynamic coefficients are considered as functions solely of the flight conditions and aircraft configuration,

$$\hat{\boldsymbol{C}}_F = \hat{\boldsymbol{C}}_F \left(\alpha, \beta, M_\infty, \delta_i, p, q, r, \dot{\alpha}, \dot{\beta} \right) \tag{2}$$

where δ_i represents any configuration-dependent information such as control-surface settings, and p, q, and r are the roll, pitch, and yaw rotation rates, respectively.[*] A more detailed representation would potentially include dependencies on altitude, propulsion, etc., which can be treated in a similar manner, but are not necessary for the current discussion. It is assumed here that for any numerical simulation each independent variable is specified exactly, while the resulting computed aerodynamic forces and moments will have associated errors and uncertainties. We thus distinguish the computed forces and moments as $\boldsymbol{C}_F$, which differ from the exact values by an error distribution: $\hat{\boldsymbol{C}}_F = \boldsymbol{C}_F + \boldsymbol{e}$.

Theoretically, the aerodynamic loads can be tabulated as functions of all the independent parameters, with suitable resolution in regions of rapid variation. In practice, the effects of the dynamic parameters, $\left(p, q, r, \dot{\alpha}, \dot{\beta} \right)$, are usually isolated using a linear expansion. Adopting $\boldsymbol{\xi}$ and $\boldsymbol{\eta}$ to represent the vectors of static and dynamic parameters respectively, we then have

$$\hat{\boldsymbol{C}}_F \left(\boldsymbol{\xi}, \boldsymbol{\eta} \right) = \boldsymbol{C}_F \left(\boldsymbol{\xi}, \boldsymbol{\eta} \right) + \boldsymbol{e} = \boldsymbol{C}_F \left(\boldsymbol{\xi} \right) |_{\boldsymbol{\eta}=0} + \frac{\partial \boldsymbol{C}_F}{\partial \boldsymbol{\eta}} \left(\boldsymbol{\xi} \right) \Delta\boldsymbol{\eta} + \boldsymbol{e}$$
$$= \boldsymbol{C}_{F_s} \left(\boldsymbol{\xi} \right) + \boldsymbol{C}_{F_d} \left(\boldsymbol{\xi} \right) \Delta\boldsymbol{\eta} + \boldsymbol{e} \tag{3}$$

---

[*]It is assumed that the rotation rates are suitably non-dimensionalized. The set of rotational parameters is often reduced using linear combinations, e.g. combining the effects of pitching and plunging as ½$(q + \dot{\alpha})$, cf. Kalviste[16].

American Institute of Aeronautics and Astronautics

In Eqn. 3 we now also have a *fit error* included in e which measures how well the linear expansion fits the data. Here, we refer to C_{F_d} as the dynamic coefficients, and C_{F_s} as the static coefficients. Note that these static coefficients are not in general identical to the results of static simulations. The motivation for Eqn. 3 is that both the static and dynamic coefficients are now only functions of the static parameters, $\boldsymbol{\xi}$, and hence easier to either tabulate or model.

As a more concrete example, we examine the pitching moment obtained from a free-oscillation simulation. For this 1-DOF simulation, the two independent parameter vectors reduce to $\boldsymbol{\xi} = \alpha$, and $\boldsymbol{\eta} = q$.[*] Simplifying Eqn. 3, and only considering pitching moment, we thus have

$$\hat{C}_m\left(\alpha, q\right) = C_{m_s}\left(\alpha\right) + C_{m_d}\left(\alpha\right)\Delta q + e \tag{4}$$

Figure 2 presents the variation of pitching moment with time and pitch rate for a representative free-oscillation simulation. The coefficients from Eqn. 4 are labeled in Fig. 2b for clarity. Both C_{m_s} and C_{m_d} are calculated directly by a linear regression against the computed data.[†] Further, modeling of the coefficients to facilitate analysis and the development of guidance and control systems is possible. For example, a linear aerodynamic model is constructed using

$$C_{m_s}\left(\alpha\right) = C_{m_\circ} + \frac{\partial C_m}{\partial \alpha}\Delta\alpha = C_{m_\circ} + C_{m_\alpha}\Delta\alpha \tag{5}$$

$$C_{m_d}\left(\alpha\right) = \frac{\partial C_m}{\partial q} = C_{m_q} \tag{6}$$

with C_{m_α} referred to as the pitch stiffness, and C_{m_q} the pitch damping. Combining Eqns. 5–6 with Eqn. 4 gives

$$\hat{C}_m\left(\alpha, q\right) = C_{m_\circ} + C_{m_\alpha}\Delta\alpha + C_{m_q}\Delta q + e \tag{7}$$

where the aerodynamic coefficients are commonly determined from a multiple linear regression.

In ballistic-range testing, the aerodynamic coefficients are not typically measured directly, but rather inferred from an assumed aerodynamic model which is fit against the measured trajectory of the test article. For example, in reducing atmospheric-entry capsule configurations, Chapman and Yates[5] assume the

---

[*]$\dot{\alpha}$ and q are equivalent for a free-oscillation motion.

[†]The uncertainty e is commonly assumed to be a normal distribution with zero mean, so the regression analysis is equivalent to a maximum likelihood estimate.

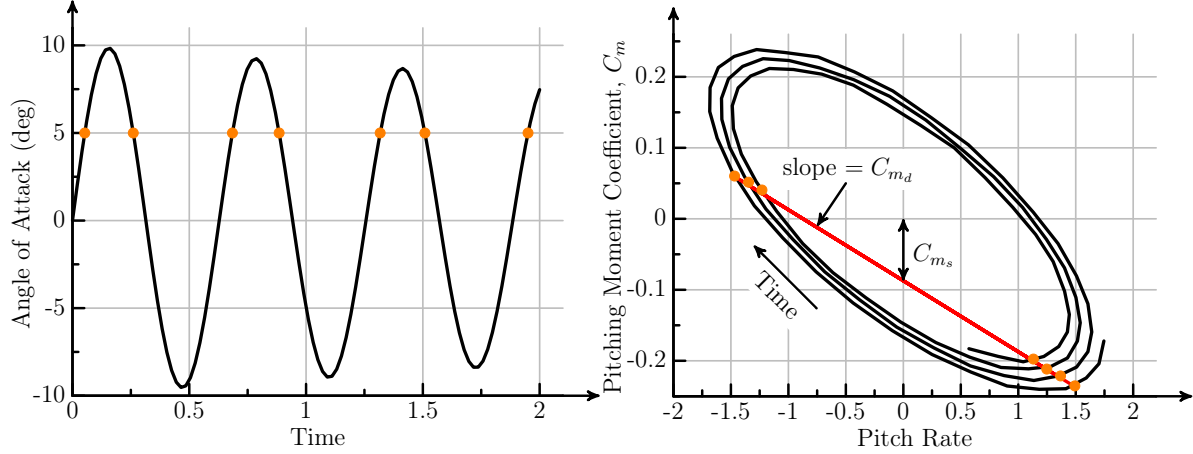American Institute of Aeronautics and Astronautics

Figure 2: Typical free-oscillation simulation data. Roughly 50 timesteps resolve each period of oscillation using a second-order numerical scheme. The $\alpha = 5°$ points are highlighted in both figures, and the static and dynamic coefficients determined from a linear regression of Eqn. 4 are shown.

following forms[*] for the static and dynamic coefficients in Eqn. 4

$$C_{m_s}(\alpha) = C_{m_\circ} + C_{m_\alpha} \sin \alpha + C_{m_{\alpha 3}} \sin^3 \alpha \tag{8}$$

$$C_{m_d}(\alpha) = C_{m_q} + \left(C_{m_q}\right)_{\alpha^2} \sin^2 \alpha \tag{9}$$

along with a data partitioning process. This data-reduction process creates a difficulty for the validation of CFD results against free-flight data. As the free-flight data-reduction methods increase in complexity, replicating them becomes impractical, so comparisons of computed and test results necessarily contain ambiguity in the reported quantities. The modeling forms are also not unique, with several plausible choices replicating the limited number $(\mathcal{O}(10))$ of experimental runs, and engineering judgement of the ballistic-range data analyst currently the deciding factor. The CFD simulations of the Orion CM in § 5 are compared against two separate experimental data reduction methods of a single ballistic range data set, as well as data from two distinct range facilities using the same data reduction process.

An *a priori* aerodynamic modeling assumption is similarly necessary to reduce CFD free-flight simulation results to aerodynamic coefficients. The current work avoids this issue by focusing solely on free-oscillation simulations where the vehicle is "pinned" through the center of mass, and only allowed to rotate in the pitch plane. The data reduction process then simplifies to a linear (dynamic) expansion in the pitch plane (e.g. Eqn. 4), where the nonlinear static and dynamic coefficients are tabulated for comparison against the nonlinear ballistic-range models.

---

[*]For simplicity, this discussion neglects contributions outside the pinned 1-DOF pitching motion, and focuses on ballistic configurations which trim about $\alpha = 0°$.

American Institute of Aeronautics and Astronautics

3 Numerical Method

Overflow provides an attractive test-bed for the current study due to the large number of turbulence models included in the standard distribution, and the ease with which new models can be added. One of the goals of this work is to evaluate the predictive capability of current engineering CFD tools for dynamic analysis. As such, the same procedure is used for each configuration analyzed in this work, varying only the physical model in isolated tests. Overflow's default central-differencing scheme with scalar artificial dissipation model is utilized throughout. The mesh resolution is determined from a grid sensitivity study at static conditions using Olsen and Coakley's k-ω Lag RANS turbulence model[17]. The k-ω-Lag model has demonstrated good accuracy for static simulations in the supersonic regime for the Apollo and Orion CM capsules[18, 19]. A typical overset, viscous mesh resulting from this resolution study contains between 9.5-11M cells. A sample cutting surface through the pitch plane of the computational mesh for the Orion CM, along with computed Mach contours at Mach 1.25, is shown in Fig. 3. Body-conforming regions are utilized to capture the boundary layer, with automatic Cartesian meshing outside these regions.
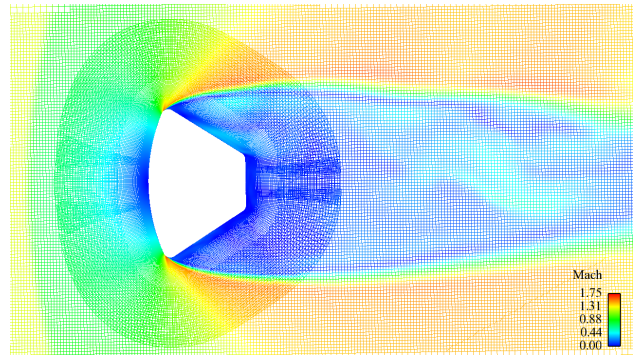

Figure 3: Overset computational mesh and Mach contours along the lateral symmetry plane for the Orion CM configuration. Volume mesh contains 11M grid points. ($M_\infty = 1.25$, $\alpha \approx 0°$, $Re_D = 1.75 \times 10^6$).

The mesh is generated automatically from the analytical outer mold-line definitions using a derivative of the Chimera Grid Tools[20] script developed by Chaderjian and Olsen[18].

The current work utilizes free-oscillation simulations where the vehicle is "pinned" through the center of mass, and only allowed to rotate in the pitch plane in response to the aerodynamic torque. This leverages the inertia of the body to filter the nonlinear response of the wake (cf. [8]), and provides an accurate model of the dynamic response. In this method, the computational mesh is fixed, and the entire domain rotates with body. The inertia and dimensions of the configurations match the ballistic-range test articles. Above Mach 1.5, the supersonic flow damps much of the unsteady wake shedding, and a time resolution of 50 timesteps per body oscillation period with the second-order backward time-integration scheme is used. Using the boundary-layer acceleration described in Appendix A, 50-100 dual-time sub-iterations are required at each timestep to converge the skin friction for this temporal resolution. Below Mach 1.5, the unsteady wake contains a broader range of scales, and a time-resolution study is necessary. The current approach uses static, unsteady simulations with varying time resolution until the prediction of axial

American Institute of Aeronautics and Astronautics

force converges. This procedure typically leads to 500 timesteps per oscillation period at the low supersonic Mach numbers. A dynamic simulation with 10M cells requires roughly 100 Itanium2 cpu-hours per oscillation cycle, and a minimum of three oscillation cycles is desired.

4   PAI-DAE

NASA's PAI-DAE project is researching methods to replace canopy decelerators with attached inflatable drag devices to increase the mass which can safely be landed during atmospheric entry, most notably on Mars, where the density of the atmosphere limits traditional decelerator technologies (cf. Hughes et al. [21]). The configuration examined here is one of a parametric series of rigid models (approximating a stacked-toroid concept) tested in the Aeroballistic Research Facility (ARF) at Eglin Air Force Base[12]. The aerodynamic coefficients are reduced from shadowgraph images using the Comprehensive Aerodynamic Data Reduction System for Aeroballistic Ranges (CADRA) software developed by Yates[22]. The pitch plane of the computational mesh for the PAI-DAE model is shown Fig. 4, along with computed Mach contours. The model is a $60°$ sphere-cone forebody, with a concave aft-body and cylindrical base. This model is chosen as it contains the greatest number of experimental datapoints (4) of the $60°$ forebody configurations tested.
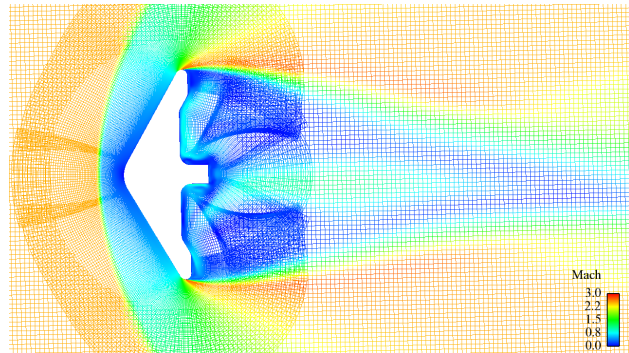

Figure 4: Overset computational mesh and Mach contours along the lateral symmetry plane for a rigid sphere-cone PAI-DAE configuration. Volume mesh contains 9.8M grid points. ($M_\infty = 2.5, \alpha \approx 0°, Re_D = 4.1 \times 10^6$).
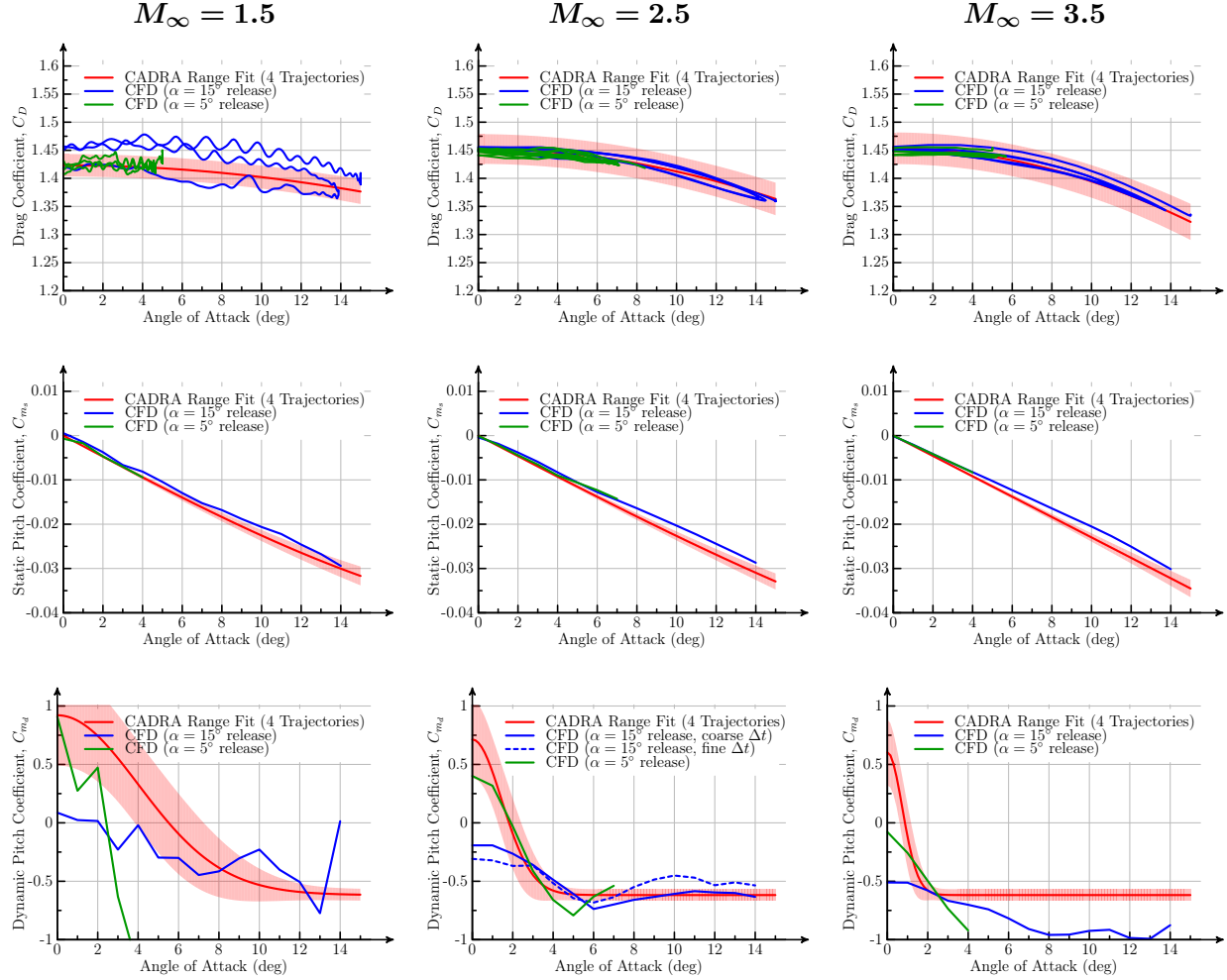
Free-oscillation simulations of the PAI-DAE configuration at supersonic conditions using the Overflow RANS solver with the Spalart-Allmaras Detached-Eddy Simulation (DES) turbulence model[23] are presented. The DES model includes the low-Reynolds-number corrections for wake flows[24]. Figure 5 compares the computed aerodynamic coefficients against data reductions from the ballistic range trajectories. Uncertainties ($\pm 3\sigma$) for the experimental regression fit are included using the error estimates from the range data and assuming a uniform error distribution. Note that these do not represent cumulative experimental uncertainties. Two separate simulations are included for each Mach number, with the body released from both $15°$ and $5°$ from the static trim point ($\alpha = 0°$). The range data includes two high-amplitude trajectories, with oscillations through $\pm 10°$ in total angle of attack, and two lower-amplitude

American Institute of Aeronautics and Astronautics

Figure 5: Predictions of the static and dynamic (C_D, C_{m_s}, and C_{m_d}) aerodynamic coefficients for a rigid sphere-cone PAI-DAE configuration at three supersonic Mach numbers. Range data is a regression fit of an assumed aerodynamic model against the trajectory data[12]. 3σ uncertainties are included for the range data regression fit by assuming a uniform error distribution.

($\alpha_{tot} < \pm 5°$) trajectories. The simulation and free-flight drag coefficient are in good agreement at all Mach numbers. The range data regression does not include a dynamic component for the drag coefficient, while the simulations indicate a noticeable hysteresis at $M_\infty = 1.5$. The oscillation of the unsteady wake is also evident in the drag variation at $M_\infty = 1.5$, and resolving this feature is required for accurate predictions. At the lower speed, the greater load increment due to the stronger wake causes oscillations in the computed damping predictions. The static pitching moment coefficient is in good agreement, though slightly underpredicts the slope of the range data regression at the higher speeds. The dynamic pitching-moment coefficient demonstrates two trends, differing with release angle of attack. The release $15°$ from the static trim point is in good agreement with the range predictions for the higher angles of attack, but

American Institute of Aeronautics and Astronautics

underpredicts the dynamic instability near the static trim point. The lower angle of attack release does predict a noticeably greater instability however. Note that at the peak amplitude of the oscillation the rotation rate is essentially zero, and the dynamic coefficient is arbitrary.

For the Mach 2.5 simulations in Fig. 5, two $\alpha = 15°$ releases are included in the dynamic coefficient, one which resolves the dynamics using roughly 50 timesteps per oscillation period, and one which matches the angular resolution of the lower angle of attack release. There are no significant differences in the predicted pitch damping with angular resolution, indicating that the changing behavior with release angle of attack is not numerical in origin. Teramoto et al. [25, 26] note similar dynamic phase delays in the pressure field about a capsule computed at transonic conditions. One of the significant differences between the low and high angle-of-attack releases is the rotation rate passing through the static trim point, with the higher-amplitude release resulting in roughly twice the pitch rate. The next section discusses physical mechanisms which lead to the change in aerodynamic damping with release angle of attack. The larger issue is the assumption inherent in commonly used aerodynamic models (including those of the ballistic range data reduction) that the dynamic coefficients are independent of rotation rate (e.g. Eqn. 3). Based on the simulation data here (and the next section), this assumption should be reconsidered, and refined models which account for a more general dynamic increment may be necessary for these nonlinear bluff-body flows.

Simulations using the delayed DES model (DDES) recently proposed by Spalart et al. [24] are included for the PAI-DAE configuration at Mach 2.5. The motivation for the DDES changes is the observation that today's more abundant computational resources lead to finer mesh resolution than used in calibrating the DES model. This often obscures the region where the LES and RANS overlap, leading to a premature (undesirable) switch to LES mode within the boundary layer. Dynamic pitch-damping results ($\alpha = 15°$ release) using DES and DDES are contrasted in Fig. 6. The DDES simulations predict a damped behavior across the angle-of-attack range, in contrast with the DES results and range predictions. The cause of the discrepancy is traced to the turbulent eddy viscosity in the wake region (cf. Fig. 7). The largest
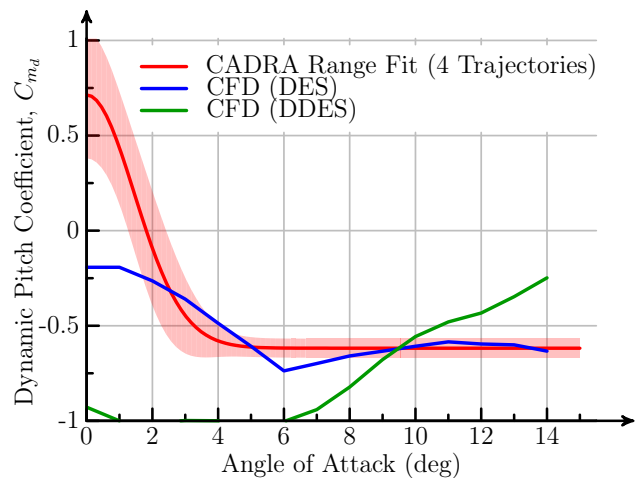

Figure 6: Variation of the pitch damping sum with angle of attack for rigid sphere-cone PAI-DAE configuration. CFD results present the dynamic coefficient, $C_{m_d}(\alpha)$. Range data is a regression fit of an assumed aerodynamic model against the trajectory data[12]. ($M_\infty = 2.5$, $Re_D = 4.1 \times 10^6$).

American Institute of Aeronautics and Astronautics

wake eddy viscosity is expected to occur in the separating shear layers, as seen in the DES simulations. The DDES model predicts a turbulent eddy viscosity in the wake region two orders of magnitude larger than the DES model, with the peak eddy viscosity in recirculation region, as opposed to the free shear layer. The DDES modification uses the local mesh spacing, wall length scale, and strain rate. In the strong wake the logic erroneously forces the model into RANS mode, leading to a greater production of turbulent eddy viscosity. Damping of the wake structure due to excessive eddy viscosity appears to be the primary cause of the discrepancy between the two hybrid-RANS simulations.

(a) S-A DDES   (b) S-A DES
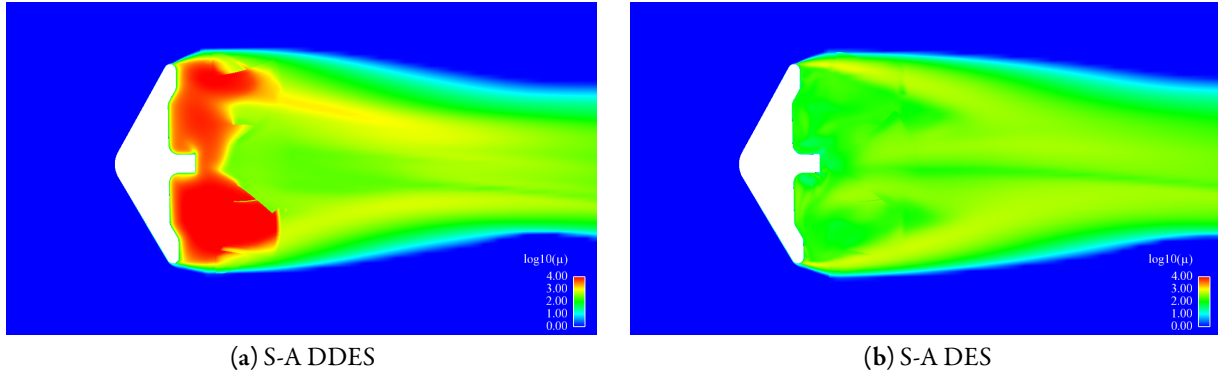
Figure 7: Snapshot of turbulent eddy viscosity contours, $\log_{10}(\mu_t/\mu_\infty)$, along the lateral symmetry plane as the PAI-DAE configuration passes through $\alpha = 0°$ during free-oscillation simulations. ($M_\infty = 2.5$, $Re_D = 4.1 \times 10^6$).

The computed aerodynamic predictions in Fig. 5 represent a cumulative cost of roughly 2000 cpu-hours on the NASA SGI Altix Columbia system (3 Mach numbers, by 2 simulations, by 300 cpu-hours per simulation). From this investment, accurate predictions of both the static and dynamic response coefficients are obtained. The dynamic simulation approach is thus computationally efficient, requiring a fraction of the resources of a typical static database approach. For inherently unsteady flows, a static database requires time-averaged, unsteady simulation results at each point in the parameter space, and does not provide any dynamic response information.

5   Orion Crew Module

Extensive ballistic-range and wind-tunnel test data exists for the Orion CM, in both lifting and non-lifting configurations, from supersonic through subsonic speeds. The comparisons here are at supersonic (approximately flight Reynolds number) conditions, for non-lifting configurations. This work focuses on comparisons with the free-flight data obtained in both the NASA Ames Hypervelocity Free Flight Aerodynamic Facility (HFFAF)[13] and the Eglin ARF[14]. In addition to comparisons between the two facilities, two distinct methods of reducing the measured trajectories to aerodynamic coefficients are avail-

able for the Eglin data: CADRA and the Aeroballistic Research Facility Data Analysis System (ARFDAS) developed by Hathaway and Whyte[27]. The range test configuration is an early Orion CM configuration with identical radii of curvature at the maximum diameter and rear shoulder (cf. Fig. 3). Two center-of-gravity locations were tested for the non-lifting configuration, and here we examine the $x_{c.g.} = 0.26D$ configuration.

A summary of the static and dynamic coefficients at $M_\infty = 1.25$ and 2.5, compared with ballistic range data reductions for the Orion CM, is presented in Fig. 8. Note that the Orion CM typically follows the Apollo coordinate convention, where the static aeroshell-forward trim location is $\alpha = 180°$, but here the results are rotated to maintain consistency with the previous section. At Mach 1.25 there are three range data reductions: the same orientation and position from the Eglin ARF reduced using CADRA and ARFDAS, and a CADRA data reduction from the Ames HFFAF. Data was not taken in the Ames facility above $M_\infty = 1.25$. Multiple trajectories, at conditions leading to both high-amplitude and low-amplitude oscillations, are available in the range data. The data follows the same trends as the PAI-DAE analysis, and only the main points are summarized again here. The drag coefficient is in good agreement with the range data reductions, and shows a hysteresis at Mach 1.25. The slope of the static pitch coefficient is slightly lower in the higher-velocity simulations, compared to the range modeling. The damping demonstrates two distinct trends with release angle of attack (rotation rate), with the lower angle of attack release showing a greater tendency towards instability (two angular resolutions are again included at $M_\infty = 2.5$). The stronger wake at Mach 1.25 leads to oscillatory damping predictions. The simulations predict a large damping coefficient at the high angles of attack for the $M_\infty = 1.25$ conditions. The rotation rate at these conditions is essentially zero however, so the value of the coefficient is arbitrary. Higher-amplitude data is necessary to get an accurate prediction for this regime. If a linear aerodynamic model is assumed for this regime, as is done in the range data reductions, the comparison is favorable. The different methods of reducing the range data, and the data gathered from different ranges, contains as much variation, especially for the dynamic damping coefficients near the static trim point and the drag coefficient at high angles of attack, as exists between the simulation data and the range predictions.

Figure 9 presents computed Mach contours and skin-friction from two Mach 2.5 simulations differing by release angle of attack. In both simulations, the snapshot captures the body passing through the static trim point during the pitch down (decreasing angle of attack) phase of the oscillation. The greater inertia of the boundary layer on the windward aeroshell (Magnus effect) due to the greater rotation rate in the higher α release delays the separation around the maximum diameter location, leading to a shock-induced separation on the smooth aft-body. The lower rotation rate separates near the location of maximum diameter, and the wake structure is much broader and stronger. This stronger wake leads to oscillations in the predicted damping coefficient, as is seen at the lower Mach numbers. The changing physical mechanisms
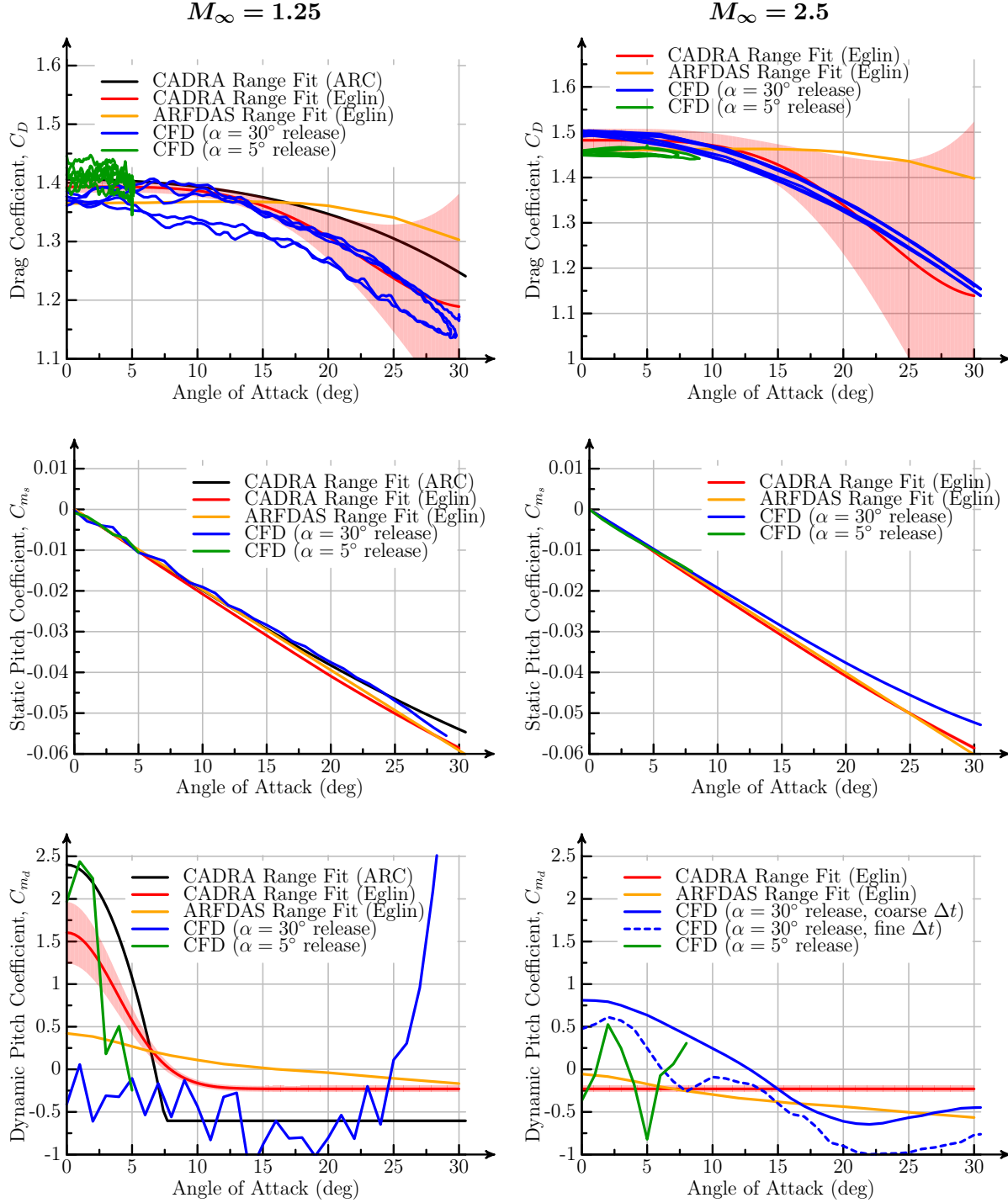
American Institute of Aeronautics and Astronautics

Figure 8: Predictions of the static and dynamic (C_D, C_{m_s}, and C_{m_d}) aerodynamic coefficients for Orion CM configuration at two supersonic Mach numbers. Range data is a regression fit of an assumed aerodynamic model against the trajectory data[12]. 3σ uncertainties are included for the range data regression fit by assuming a uniform error distribution.
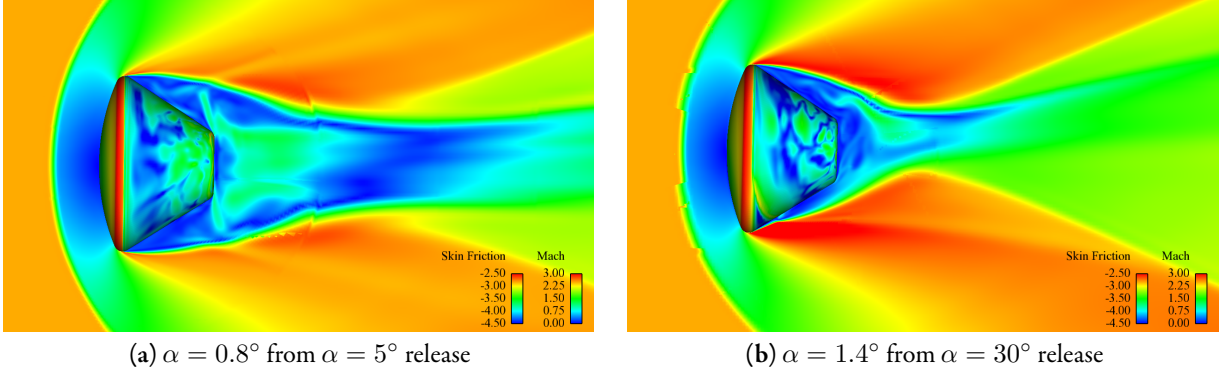
American Institute of Aeronautics and Astronautics

(a) $\alpha = 0.8°$ from $\alpha = 5°$ release   **(b)** $\alpha = 1.4°$ from $\alpha = 30°$ release

Figure 9: Snapshot of Mach contours along the lateral symmetry plane as the Orion CM passes through $\alpha = 0°$ during free-oscillation simulations. Viscous surface colored by $\log|C_f|$. Both simulations are pitching down (decreasing angle of attack). The Magnus effect in the higher α release (higher rotation rate) delays the separation around the maximum diameter location leading to a shock-induced separation on the lower surface. ($M_\infty = 2.5$, $Re_D = 3.5 \times 10^6$).

with rotation rate are not reflected in common aerodynamic modeling approaches.

6   Summary and Future Topics

The use of viscous, free-oscillation CFD simulations to predict the aerodynamic behavior of capsule shapes in the supersonic speed regime provides accurate predictions of both the static and dynamic co-efficients needed for aerodynamic modeling. The predictive capability uses a static grid and temporal-refinement strategy, along with the Spalart-Allmaras DES turbulence model. The simulation results are validated for two novel configurations: an idealized inflatable decelerator concept from the PAI-DAE project, and the Orion CM. Analysis of the results indicates that the typical nonlinear, bluff-body behavior is characterized by a rate-dependent dynamic response, which is not currently accounted for in common aerodynamic models. With this dynamic simulation approach, an aerodynamic performance database is generated using a fraction of the time required to build a typical static database, while in addition providing the dynamic response information needed for accurate modeling.

Future research is aimed at two distinct areas: novel applications and development of a free-flight data reduction capability. First, the rigid sphere-cone PAI-DAE configuration examined here is not representative of a tension-cone flexible decelerator structure. Applying the procedure validated here to a tension-cone structure, both rigid and flexible, is part of an ongoing research project. Similarly, the Orion CM is nominally a lifting body staged to subsonic speeds before the drogue-chute deployment. Analysis of the Orion CM under subsonic lifting conditions is likewise part of ongoing work.

The second research topic is the development of a general method for reducing free-flight simulation

American Institute of Aeronautics and Astronautics

data to an aerodynamic model. The current free-oscillation approach has several attractive features, but a free-flight capability will provide greater efficiency for the process, and the ability to predict general dynamic model parameters.

Acknowledgments

References

[1] Redd, B., Olsen, D. M., and Burton, R. L., "Relationship Between the Aerodynamic Damping Derivatives Measured as a Function of Instantaneous Angular Displacement and the Aerodynamic Damping Derivatives Measured as a Function of Oscillation Amplitude," NASA TN D-2855, June 1965.

[2] Moseley, Jr., W.C., Graham, R.E., and Hughes, J.E., "Aerodynamic Stability Characteristics of the Apollo Command Module," NASA TN D-4688, August 1968.

[3] Steinberg, S., Uselton, B.L., and Siemers, III, P.M., "Viking Pitch Damping Derivatives as Influenced by Support Interference and Test Techniques," *Journal of Spacecraft and Rockets*, 10(7):443–449, July 1973.

[4] Sammonds, R.I. and Kruse, R. L., "Viking Entry Vehicle Aerodynamics at M = 2 in Air and Some Preliminary Test Data for Flight in CO_2 at M = 11," NASA TN D-7974, June 1975.

[5] Chapman, G.T. and Yates, L.A., "Dynamics of Planetary Probes: Design and Testing Issues," AIAA Paper 1998-0797, January 1998.

[6] Chapman, G.T. and Yates, L.A., "Limit Cycle Analysis of Planetary Probes," AIAA Paper 1999-0496, January 1999.

[7] Winchenbach, G.L., Chapman, G.T., Hathaway, W., Ramsey, A., and Berner, C., "Dynamic Stability of Blunt Atmospheric Entry Configurations," *Journal of Spacecraft and Rockets*, 39(1):49–55, January 2002.

[8] Murman, S.M. and Aftosmis, M.J., "Dynamic Analysis of Atmospheric-Entry Probes and Capsules," AIAA Paper 2007-0074, January 2007.

[9] Buning, P.G., Chiu, I.T., Obayashi, S., Rizk, Y.M., and Steger, J.L., "Numerical Simulation of the Integrated Space Shuttle Vehicle in Ascent," AIAA Paper 88-4359, 1988.

[10] Jespersen, D.C., Pulliam, T.H., and Buning, P.G., "Recent Enhancements to OVERFLOW," AIAA Paper 97-0644, January 1997.

[11] Nichols, R.H., Tramel, R.W., and Buning, P.G., "Solver and Turbulence Model Upgrades to OVER-FLOW 2 for Unsteady and High-Speed Applications," AIAA Paper 2006-2824, 2006.

[12] Yates, L.A. and Chapman, G.T., "Analysis of Data from Ballistic Range Tests of PAI-DAE Vehicles," Aerospace Computing, Inc., Report, November 2007.

[13] Brown, J. D., Bogdanoff, D. W., Yates, L. A., and Chapman, G.T., "Free-Flight Dynamic Aero Data for a Lifting CEV Capsule," AIAA Paper 2008-1232, January 2008.

[14] Yates, L.A. and Chapman, G.T., "Analysis of Data from Ballistic Range Tests for an Untrimmed CEV Model," Aerospace Computing, Inc., Report, December 2006.

[15] "Aerodynamic Results: NASA - CEV Test Configuration," Arrow Tech Associates, Report ARO-07-0111, January 2007.

[16] Kalviste, J., "Use of Rotary Balance and Forced Oscillation Test Data in Six Degrees of Freedom Simulation," AIAA Paper 1982-1364, 1982.

[17] Olsen, M.E. and Coakley, T.J., "The Lag Model, a Turbulence Model for Non Equilibrium Flows," AIAA Paper 2001-2564, June 2001.

[18] Chaderjian, N.M. and Olsen, M.E, "Grid Resolution and Turbulence Model Effects on Space Capsule Navier-Stokes Simulations," AIAA Paper 2007-4562, June 2007.

[19] Olsen, M.E, Chaderjian, N.M., Lillard, R.P., Greathouse, J.S., and Coakley, T.J., "Numerical Study of Massively Separated Flows," AIAA Paper 2007-1412, January 2007.

[20] Chan, W. M., Gomez, R.J., Rogers, S.E., and Buning, P.G., "Best Practices in Overset Grid Generation," AIAA Paper 2002-3191, June 2002.

American Institute of Aeronautics and Astronautics

[21] Hughes, S.J., Dillman, R.A., Starr, B.R., Stephan, R.A., Lindell, M.C., Player, C.J., and Cheatwood, F.M., "Inflatable Re-entry Vehicle Experiment (IRVE) Design Overview," AIAA Paper 2005-1636, 2005.

[22] Yates, L.A., "A Comprehensive Aerodynamic Data Reduction System for Aeroballistic Ranges," Wright Laboratory, Technical Report 96-7059, October 1996.

[23] Spalart, P. R., "Strategies for Turbulence Modeling and Simulations," *International Journal of Heat and Fluid Flow*, 21:252–363, 2000.

[24] Spalart, P. R., Deck, S., Shur, M.L., Squires, K.D., Strelets, M.Kh., and Travin, A., "A New Version of Detached-Eddy Simulation, Resistant to Ambiquous Grid Densities," *Theoretical Computational Fluid Dynamics*, 20:181–195, 2006.

[25] Teramoto, S., Hiraki, K., and Fujii, K., "Numerical Analysis of Dynamic Stability of a Reentry Capsule at Transonic Speeds," *AIAA Journal*, 39(4):646–653, 2001.

[26] Teramoto, S. and Fujii, K., "Mechanism of Dynamic Instability of a Reentry Capsule at Transonic Speeds," *AIAA Journal*, 40(12):2467–2475, 2002.

[27] Hathaway, W.H. and Whyte, R.H., "Aeroballistic Research Facility Free Flight Data Analysis Using the Maximum Likelihood Method," Air Force Armament Laboratory, Technical Report 79-98, December 1979.

A   Boundary-Layer Convergence Acceleration

This appendix describes a method of specifying the iterative timestep within the Overflow solver. When appropriate, specific Overflow input parameters are noted using a fixed-width font, e.g. `ITIME=3`.

For viscous, moving-body simulations using an iterative method, such as the dual-time scheme in Overflow, convergence of the boundary layer is a limiting factor in the efficiency of the numerical scheme. At each timestep the boundary layer, and any separated regions, must react to the new body orientation. Simulations of high-speed flows using Overflow typically use an inviscid CFL condition throughout to ensure numerical stability. Within the boundary layer, this inviscid timestep is overly conservative. Common methods of overcoming this limitation involve a local cell Reynolds number to adjust the timestep in viscous regions.[*] The development of a cell Reynolds number timestep formulation must be consistent with the inviscid formulation. Overflow uses a monotone inviscid CFL condition (`ITIME=3`) where

$$\text{CFL} = \frac{\sum_{faces}(|\boldsymbol{u}| + a)\Delta t}{\Delta x} \tag{10}$$

with $\boldsymbol{u}$ the velocity and a the sonic speed. For the node-centered, finite-difference formulation used in Overflow this takes the form

$$\text{CFL} = \frac{\sum_{j,k,l}(|u_t + \boldsymbol{u} \cdot \boldsymbol{\kappa}| + a\,|\boldsymbol{\kappa}|)\Delta t}{\mathcal{V}} \tag{11}$$

where $\boldsymbol{\kappa}$ are the appropriate grid metrics, $\mathcal{V}$ is the cell volume, and the summation occurs over each computational coordinate j, k, l.

A local cell Reynolds number based on the computational timescale is defined as

$$Re_{\Delta t} = \frac{u(u\Delta t)}{\nu} \tag{12}$$

Applying this again to the node-centered, finite-difference formulation, and choosing velocity and length scales consistent with the inviscid monotone CFL definition gives

$$Re_{\Delta t} = \left(\frac{Re_\infty}{M_\infty}\right)\frac{\left[\sum_{j,k,l}(|u_t + \boldsymbol{u} \cdot \boldsymbol{\kappa}|)\right]^2 \Delta t}{\nu \mathcal{V}^{4/3}} \tag{13}$$

---

[*]The von Neumann number is the reciprocal of a cell Reynolds number.

The scale factor $\frac{Re_\infty}{M_\infty}$ arises from the non-dimensionalization used by Overflow, and ν includes both the laminar and turbulent eddy viscosity. For regions where the viscous stresses are negligible, the cell Reynolds number is very large. As the cell Reynolds number approaches unity, viscous stresses become commensurate with the pressure. In the near-wall region the cell Reynolds number approaches zero as the viscous wall stress dominates.

The timestep formulation is modified such that

$$\text{CFL}_\nu = \text{CFL}\sqrt{\frac{10}{Re_{\Delta t}}} \qquad \Longleftrightarrow \quad Re_{\Delta t} < 10 \tag{14}$$

so that any local cell Reynolds number below 10 will amplify the timestep. This method is specified as `ITIME=4` in the Overflow namelist inputs. The variation of this viscous formulation through the boundary layer is examined for a transonic bump flow (cf. Fig. 10a). The normalized velocity and viscous timescale variation are plotted in Fig. 10 for both attached and separated flow regions. In the attached flow the timestep smoothly increases, matching the velocity profile. In the separated flow region the timescale reacts to the local flow properties, and restricts the timestep passing through the reversed flow. In both flow regions the timestep near the wall is $\mathcal{O}(10^3)$ times greater than the inviscid CFL condition alone. This increase in timestep allows the boundary layer to develop at a rate commensurate with the outer inviscid flow, increasing the convergence rate for both the viscous and pressure loads.

As the cell Reynolds number, Eqn. 13, includes the turbulent eddy viscosity, the formulation is at the mercy of the turbulence model. In regions away from the wall, flow separation or strong gradients can lead to the turbulence model predicting extremely large values of eddy viscosity. This large eddy viscosity leads to a low cell Reynolds number, triggering the timestep amplification. In many such regions the grid does not have sufficient support to accurately resolve a viscous stress, and amplifying the timestep would lead to numerical instability. To eliminate this possibility, a DES cell length scale[23] is used to further discriminate between the near-wall and inviscid regions.

The performance of the boundary-layer acceleration is demonstrated using an Onera M6 transonic wing at $\alpha = 4°$, conditions which contain a shock-induced separation region on the outboard, upper-surface of the wing (cf. Fig. 11). The convergence of the skin-friction drag using a timestep scaled by the cell volume (`ITIME=1, DT=0.025, CFLMIN=2`), the inviscid CFL condition (`ITIME=3, CFLMAX=5`), and the boundary-layer acceleration approach (`ITIME=4, CFLMAX=5`) are presented in Fig. 12. The skin friction converges to an asymptotic value several hundred iterations faster than the other methods using the boundary layer amplification, without a loss in robustness.
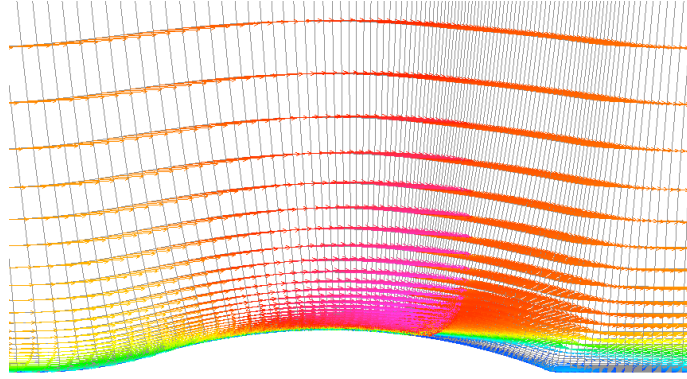
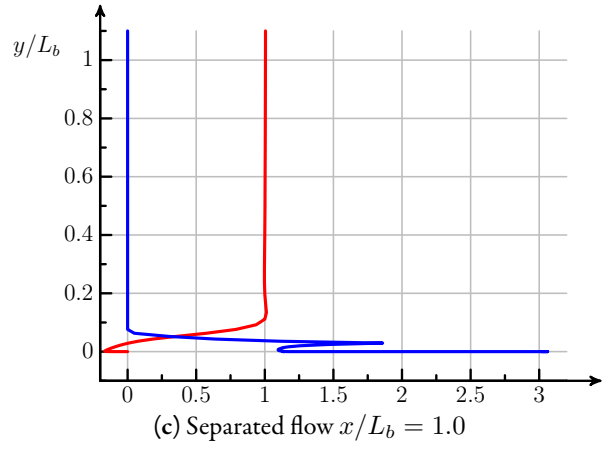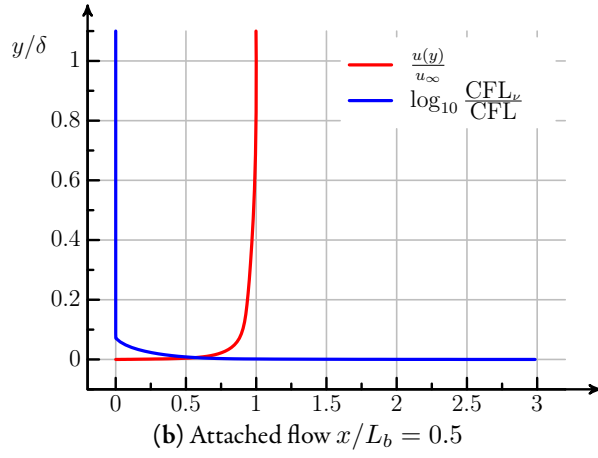(a) Velocity vectors colored by velocity magnitude.

(b) Attached flow $x/L_b = 0.5$

(c) Separated flow $x/L_b = 1.0$

Figure 10: Variation of the velocity and viscous CFL scaling through the near-wall region for the 2D transonic bump simulation. ($M_\infty = 0.875$, $Re_{L_b} = 2.76 \times 10^6$).
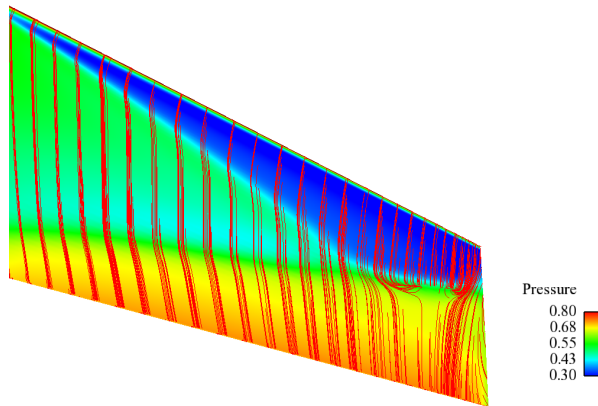
Figure 11: Surface pressure and limited streamlines for the Onera M6 wing. ($M_\infty = 0.836, \alpha = 4°, Re_b = 18$ x 10^6).

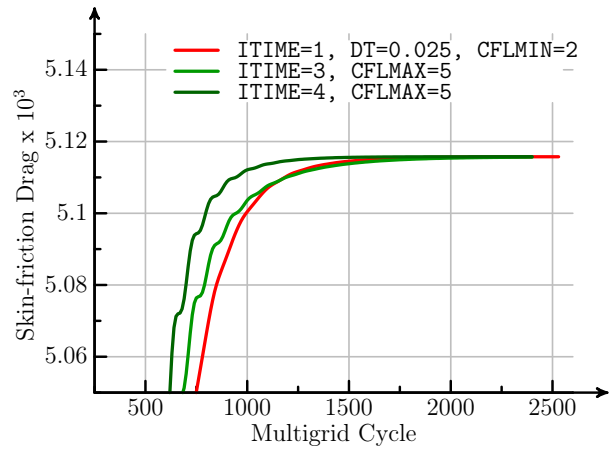**Figure 12:** Skin-friction convergence for the Onera M6 wing. ($M_\infty = 0.836, \alpha = 4°, Re_b = 18$ x 10^6).

American Institute of Aeronautics and Astronautics